Naval Research Laboratory

Washington, DC 20375-5320

NRL/MR/5650--08-9101

Analysis of Fiber-Optic Links for HF Antenna Remoting

Vincent J. Urick

Photonics Technology Branch
Optical Sciences Division

John Diehl

SFA, Inc.
Crofton, Maryland

Alex Hastings

Photonics Technology Branch
Optical Sciences Division

Christopher Sunderman

SFA, Inc.
Crofton, Maryland

Jason D. McKinney
Preetpaul S. Devgan
James L. Dexter
Keith J. Williams

Photonics Technology Branch
Optical Sciences Division

March 18, 2008

REPORT DOCUMENTATION PAGE

Form Approved
OMB No. 0704-0188

1. REPORT DATE *(DD-MM-YYYY)*
18-03-2008

2. REPORT TYPE
Memorandum Report

3. DATES COVERED *(From - To)*
01 Oct 2007 - 19 Dec 2007

4. TITLE AND SUBTITLE
Analysis of Fiber-Optic Links for HF Antenna Remoting

5a. CONTRACT NUMBER

5b. GRANT NUMBER

5c. PROGRAM ELEMENT NUMBER

6. AUTHOR(S)
Vincent J. Urick, John Diehl*, Alex Hastings, Christopher Sunderman*, Jason D. McKinney, Preetpaul S. Devgan, James L. Dexter, and Keith J. Williams

5d. PROJECT NUMBER

5e. TASK NUMBER
EW-271-003

5f. WORK UNIT NUMBER
6259

7. PERFORMING ORGANIZATION NAME(S) AND ADDRESS(ES)
Naval Research Laboratory, Code 5652
4555 Overlook Avenue, SW
Washington, DC 20375-5320

*SFA, Inc.
2200 Defense Highway
Crofton, MD 21114

8. PERFORMING ORGANIZATION REPORT NUMBER
NRL/MR/5650--08-9101

9. SPONSORING / MONITORING AGENCY NAME(S) AND ADDRESS(ES)
Office of Naval Research
875 North Randolph Street
Arlington, VA 22203-1995

10. SPONSOR / MONITOR'S ACRONYM(S)
ONR

11. SPONSOR / MONITOR'S REPORT NUMBER(S)

12. DISTRIBUTION / AVAILABILITY STATEMENT
Approved for public release; distribution is unlimited.

13. SUPPLEMENTARY NOTES

14. ABSTRACT
This report describes a fiber-optic link design for the long-haul remoting of HF antennas. The link presented here is intended for remoting the antenna element a distance upwards of 7.0 km (4.3 mi) but the theoretical treatment allows for the design and analysis of links for greater stand offs. The analysis is carried out using well-established theory and verifying expermental data are employed throughout. A complete list of supporting references is also provided. The fiber-optic link performance is summarized as a 7-km point-to-point link with a single radio-frequency input and output having the following performance metrics over the 2-30 MHz range: –0.86 dB gain, 21 dB noise figure, 116.7 dB-Hz $^{2/3}$ spurious-free dynamic range above 1-Hz bandwidth, and 0.14°/°C phase stability over temperature. These metrics are for the fiber-optic link only and throughout the report we compare this performance to various all-electric systems demonstrating that the fiber link is suitable for HF applications.

15. SUBJECT TERMS
Fiber optics   Analog photonics   HF photonics

16. SECURITY CLASSIFICATION OF: a. REPORT	b. ABSTRACT	c. THIS PAGE	17. LIMITATION OF ABSTRACT	18. NUMBER OF PAGES	19a. NAME OF RESPONSIBLE PERSON
Unclassified	Unclassified	Unclassified	UL	27	Vincent J. Urick
					19b. TELEPHONE NUMBER *(include area code)* (202) 767-9352

Standard Form 298 (Rev. 8-98)
Prescribed by ANSI Std. Z39.18

TABLE OF CONTENTS

ANALYSIS OF FIBER-OPTIC LINKS FOR HF ANTENNA REMOTING

EXECUTIVE SUMMARY

This report describes a fiber-optic link design for the long-haul remoting of HF antennas. The link presented here is intended for remoting the antenna element a distance up to 7.0 km (4.3 mi) but the theoretical treatment allows for the design and analysis of links for greater stand offs. The analysis is carried out using well-established theory and verifying experimental data are employed throughout. A complete list of supporting references is also provided. The fiber-optic link performance is summarized as a 7-km point-to-point link with a single radio-frequency input and output having the following performance metrics over the 2-30 MHz range: −0.86 dB gain, 21 dB noise figure, 116.7 dB·Hz$^{2/3}$ spurious-free dynamic range above 1-Hz bandwidth, and 0.14°/°C phase stability over temperature. These metrics are for the fiber-optic link only and throughout the report we compare this performance to various all-electric systems demonstrating that the fiber link is suitable for HF applications.

Manuscript approved December 21, 2007

ANALYSIS OF FIBER-OPTIC LINKS FOR HF ANTENNA REMOTING

1 INTRODUCTION

Direction-finding (DF) antenna arrays have been in use and heavily researched since World War II [1]-[4]. Wullenweber-type circular dipole antenna arrays (CDAAs) operating in the high-frequency range (HF, 2-30 MHz) remain an important technology for the Navy, as evidenced by the AN/FRD-10 and PUSHER systems [5],[6]. In some cases, it would be advantageous to remote a CDAA distances upwards of 7 km. As has been demonstrated in numerous other instances, such as in radio astronomy [7]-[9], fiber-optic links are ideal for remoting antennas and antenna arrays at these distances. Optical fiber offers electrical isolation between the array elements and any signal processing electronics at the distal end of the link. For an analog link, the signal loss in fiber is on the order of 0.5 dB/km at any radio frequency, which is orders-of-magnitude better than electrical cabling. Analog optical links also offer the advantage of simplicity at the antenna-side of the link as opposed to their digital counterparts. The importance of this simplicity is demonstrated explicitly in [9] where the mean time between failure (MTBF) for an analog optical link is shown to be almost four times higher than a digital optical link for outdoor antenna-remoting applications. For these reasons, we will concentrate on an analog optical link for remoting a CDAA.

In this report, we concentrate on the analysis of a CDAA employing analog optical remoting such as shown in Fig. 1. In this configuration, an *N*-element array is connected via fiber-optic cabling to a signal analysis station. A buried fiber trunk comprises the majority of the transmission distance, which we assume to be at most 6.7 km. Each element is connected to the fiber trunk with individual fiber runs of no more than 300 m each. Here, we predict the performance of such an optically-remoted array in terms of radio-frequency (RF) gain, RF noise figure and spurious-free dynamic range. In Section 2, a proposed link design is presented and compared to RF back-to-back performance. In Section 3 the fiber effects in such a link are addressed. The work is summarized in Section 4. Throughout, we assume a link with a total length of 7 km and an RF range of 2-30 MHz.

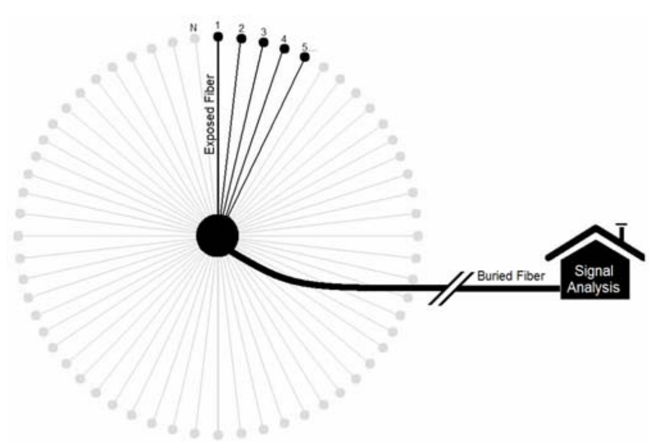

Fig. 1. The layout for an optically-remoted *N*-element circular dipole antenna array for direction-finding applications.

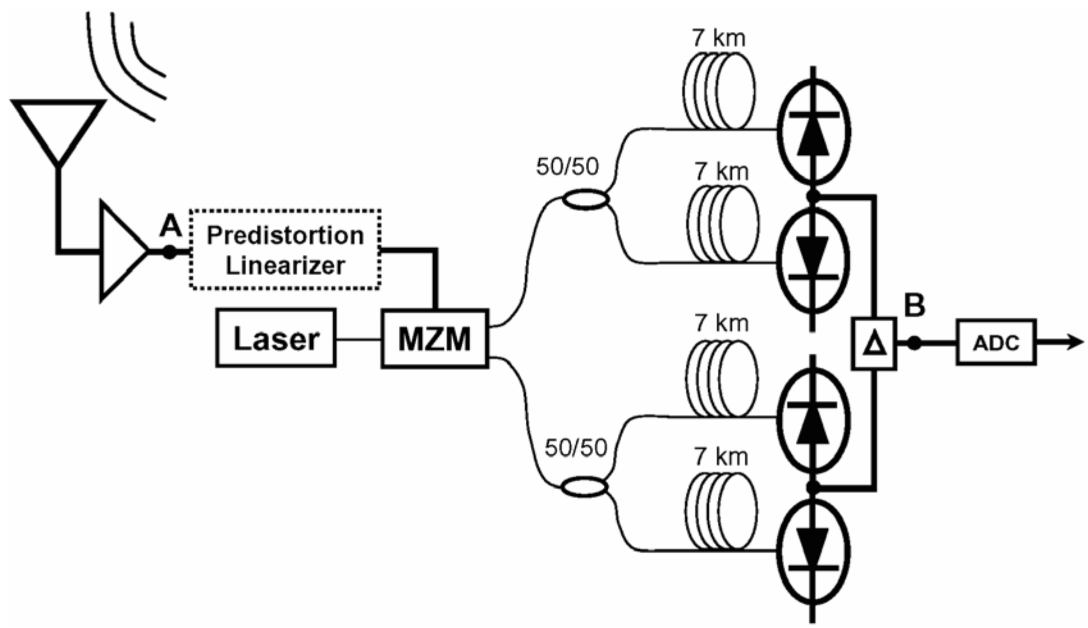

Fig. 2. The architecture for a four-fiber antenna-remoting analog optical link including the RF front and back end. The bold black lines designate electronic paths and the optical paths are shown by lighter lines. The optical link comprises a laser, a dual-output Mach-Zehnder modulator (MZM), two 50/50 fused fiber couplers, four 7-km rums of fiber, and four p-i-n photodiodes. The photodiodes are wired to sum photocurrents on a common MZM output and difference between the complimentary MZM outputs. A predistortion linearizer can be employed on the input to the MZM to increase performance. The back-to-back electrical link, designated by points A and B, includes a single antenna element, an electronic preamplifier, and an analog-to-digital converter (ADC).

2 LINK DESIGN

A four-fiber analog fiber-optic link is shown in Fig. 2 as it would be employed to remote a single element of a DF array. For an array with *N* elements, *N* links as shown in Fig. 2 would be employed, dictating that a fiber trunk with 4*N* fibers would be required. Shown also in Fig. 2 are the RF components including an antenna element, an electronic preamplifier, and an analog-to-digital converter. The back-to-back electrical link (achieved by connecting points A and B in Fig. 2) is an architecture, to the authors' knowledge, that is representative of a typical HF DF system. There is no standard RF link for such applications but the analysis below can be employed to any set of RF components. The analog fiber-optic link comprises a laser, a dual-output electro-optic Mach-Zehnder modulator (MZM), two 50/50 couplers, four phase-matched 7-km runs of fiber, and four p-i-n photodiodes. As described in [10], the two outputs of the MZM are 180° out of phase in the RF domain; the photodiode pairs are connected to add on a common MZM arm and wired to subtract the outputs from each arm. Finally, the fiber-optic link can incorporate a predistortion linearizer at the MZM RF input. For this report, we will analyze the performance of the RF back-to-back link and the performance with the linearized and unlinearized fiber-optic link inserted.

For the analysis that follows we employ the standard RF cascade equations for the performance metrics of RF gain (*G*), RF noise figure (*NF*), n^{th}-order output intercept point (*OIPn*) and n^{th}-order input intercept point (*IIPn*) [11]-[13]:

$$G = \prod_{p=1}^{m} G_p \tag{1.1}$$

$$NF = NF_1 + \sum_{\substack{i=2 \\ m\geq 2}}^{m} \left(\frac{NF_i - 1}{\prod_{p=1}^{i-1} G_p} \right) \tag{1.2}$$

$$OIPn = \left\{ \sum_{\substack{i=1 \\ m\geq 2}}^{m-1} \left[\left(OIPn_i \prod_{p=i+1}^{m} G_p \right)^{(1-n)/2} \right] + OIPn_m{}^{(1-n)/2} \right\}^{2/(1-n)} \tag{1.3}$$

$$IIPn \equiv \frac{OIPn}{G}, \tag{1.4}$$

where m is the number of stages in the cascade. In addition to Eqs. (1.3) and (1.4), we can write the expressions for the intercept points in terms of the output power at the fundamental P_f and the output power at the n^{th}-order distortion P_n as

$$OIPn = \left(\frac{(P_f)^n}{P_n} \right)^{1/(n-1)} = G_f \cdot IIPn \tag{1.5}$$

where $G_f = G$ is the RF gain at the fundamental frequency. Although not of significant importance in this treatment, Eq. (1.5) is extremely useful in experimental analysis and we include it here for completeness. The typical performance metrics of interest for an RF system are the gain, noise figure and spurious-free dynamic range (*SFDR*). We can write *SFDR* in the following two forms

$$SFDR_n\left(\mathrm{Hz}^{(n-1)/n}\right) = \left(\frac{OIPn}{N_{out}} \right)^{(n-1)/n} \tag{1.6}$$

$$SFDR_n\left(\mathrm{Hz}^{(n-1)/n}\right) = \left(\frac{IIPn}{NF \cdot k_B T} \right)^{(n-1)/n}, \tag{1.7}$$

where N_{out} is the output noise power spectral density and we have used the definition of noise figure, $NF \equiv N_{out}/(G k_B T)$ with k_B as Boltzmann's constant and T the temperature. Equations (1.1)-(1.4) and (1.7) can be easily programmed into MATLAB to facilitate the speedy analysis of an RF cascade, as we have done for the cases of $n = 2$ and $n = 3$ in the Appendix.

In order to utilize the above equations we must know the metrics for each stage in Fig. 2. We start with the analysis of the RF back-to-back, which has two analog stages if the antenna itself is neglected. The first stage is the RF preamplifier, which we take as being an AML Communications Model AR01003251X with G = 21 dB, NF = 5.5 dB, $OIP2$ = 100 dBm and $OIP3$ = 52 dBm. The second "analog" stage is the ADC. For the ADC we assume a Ten-Tec RX-331 Digital HF Receiver with G = 10 dB, NF = 10 dB, $OIP2$ = 110 dBm and $OIP3$ = 30 dBm. We can use these numbers with those for the preamplifier to calculate the RF back-to-back performance as G = 31.0 dB, NF = 5.6 dB, $SFDR_2$ = 120.7 dB·Hz$^{1/2}$ and $SFDR_3$ = 111.6 dB·Hz$^{2/3}$.

For the unlinearized optical link, we assume a 19-dBm distributed feedback (DFB) semiconductor laser (EM4, Inc. Model EM4253-80) and an MZM with a 3-dB insertion loss and a 4.5-V V_π (Eospace Model AZ-1×2-0K5-10-PFU-SFU-UL) for the optical transmitter. This configuration allows for a 10-dBm launch power into each 7-km fiber span, which is just below the stimulated Brillouin scattering threshold. Stimulated Brillouin scattering (SBS) [14] is a fiber nonlinearity that limits the amount of optical power that can be launched into a fiber-optic cable. Operating at or beyond the SBS threshold results in a compressed optical response as well as increased noise in the HF range at the link output, necessitating the need for multiple fibers in the link design. Assuming a fiber loss of 0.2 dB/km for an optical signal and a photodiode responsivity of 0.9 A/W (Applied Optronics PD1000-FA-10-HB), we will have 6.5 mA per photodiode at the output for a total DC photocurrent of $I_{\rm dc}$ = 26 mA. Given the parameters $I_{\rm dc}$ and V_π, we can then determine the link performance from well-known equations. Assuming shot-noise-limited performance, achieved via balanced detection [10],[15], the theoretical performance for the photonic link, neglecting photodiode nonlinearities, is given by [16]

$$G = \left(\frac{I_{\rm dc}}{V_\pi}\right)^2 \pi^2 Z_{\rm in} Z_{\rm out} \tag{1.8}$$

$$NF_{\rm shot} = \frac{V_\pi^2}{I_{\rm dc}} \cdot \frac{2e}{\pi^2 k_B T Z_{\rm in}} \tag{1.9}$$

$$OIP2 \to \infty \tag{1.10}$$

$$OIP3_{\rm imd3} = 4 I_{\rm dc}^2 Z_{\rm out} \tag{1.11}$$

$$OIP3_{\rm 3h} = 12 I_{\rm dc}^2 Z_{\rm out} \tag{1.12}$$

where e is the electron charge constant, $k_{\rm B}$ is Boltzmann's constant, T is the temperature, and $Z_{\rm in}$ and $Z_{\rm out}$ are the input and output impedances, respectively. Using the values $I_{\rm dc}$ = 26 mA, V_π = 4.5 V, T = 290 K and $Z_{\rm in} = Z_{\rm out}$ = 50 Ω, we have G = –0.86 dB, NF = 21.0 dB, and $OIP3$ = 21.3 dBm. Here we take the third-order intercept corresponding to third-order intermodulation distortion as given by Eq. (1.11); the $OIP3$ due to third harmonics is given by Eq. (1.12) because it is often easier to measure in multi-octave systems. (In general, $OIP3_{\rm imd3} = OIP3_{\rm 3h}$ – 4.8 dB.) In practice, the second-order distortion of a photonic link will be non-zero and is often limited by photodiode nonlinearities. While much research has been done on photodiode nonlinearities [17]-[26], there is no general analytical model for the distortion they introduce. Rather, experiment must determine the performance and we now turn to some data for photodiode second-harmonic distortion.

Shown in Fig. 3 are measured data for second harmonic distortion in a fiber-optic link employing PD1000 photodiodes as shown in Fig. 2 without the 7-km span. The second harmonic is plotted as a function of bias voltage on the MZM for single-arm (single MZM output) and balanced (both MZM outputs) configurations. In this case, the second harmonic at 10 MHz due to a 5-MHz fundamental frequency is easier to measure than the second-order intermodulation distortion, but the relationship $OIP2_{\rm imd2} = OIP2_{\rm 2h}$ – 6 dB can be used to convert to the intermodulation response. As shown in Fig. 3, the second harmonic reaches a minimum at the

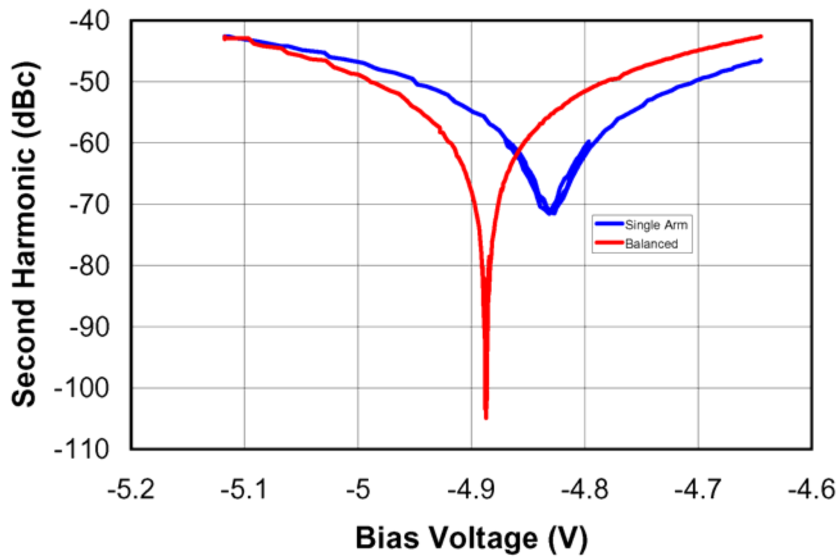

Fig. 3. The measured second harmonic response as a function of MZM bias in a link similar to that shown in Figure 2. For dual MZM outputs (red), a 29-dB suppression of second harmonic is observed as compared to a single MZM output (blue).

quadrature-bias voltage. For a single arm the null is at −76 dBc for a −5 dBm fundamental power, which is reduced to −105 dBc for a 0 dBm fundamental with the balanced architecture. The DC photocurrent is 6.5 mA per detector in both cases. Using Eq. (1.5), we can predict the *OIP*2 due to the second harmonic as 66 dBm and 105 dBm for the single arm and balanced architectures, respectively. The significant 39-dB increase in *OIP*2 is not due to the array gain of using multiple nonlinear devices (20log(*N*), where *N* is the number of elements, is the expected increase), but rather because the even-order distortion is canceled when the photocurrents are subtracted as shown in Fig. 2. The data in Fig. 3 therefore represent a cancellation on the order of 39 – 20log(2) = 33 dB. (Note here that we used $N = 2$ rather than $N = 4$ because the single arm data employ two detectors. We would use $N = 4$ when comparing the performance of one detector that that of the entire four-detector architecture.)

To describe the cancellation of photodetector nonlinearities more explicitly, we employ the data in Fig. 4. Shown in Fig. 4 are measured time-domain waveforms at the link output for each of the MZM outputs. The fundamentals at 2.5 MHz are in phase and the second harmonics are 180° out of phase, clearly demonstrating that the signal from each arm will add whereas the distortion at the second harmonic will cancel. To confirm that the second-harmonic distortion shown in Fig. 4 are due to the photodiodes, we observe that *OIP*2 = 65.0 dBm for the data shown in red and *OIP*2 = 66.5 dBm for the data in black. For these data $I_{dc} \cong 33$ mA per diode. (The high photocurrent was required in order to measure the second harmonics on the oscilloscope.) These results were obtained by using the measured peak-to-peak voltages, Eq. (1.5) and the equation $P_{\mathrm{rf}} = \left(V_{\mathrm{p-p}}^2 / \left(8 Z_{\mathrm{out}}\right)\right)$ where P_{rf} is the RF power delivered to a load Z_{out} by a sinusoid with peak-to-peak voltage $V_{\mathrm{p-p}}$. Both of the *OIP*2's agree closely with that measured for single arm as shown in Fig. 3, which was obtained using an electrical spectrum analyzer with $I_{dc} = 6.5$ mA per diode, as is expected if the photodiode were the nonlinear device causing the distortion.

In terms of system performance it is desirable that the even-order distortion due to the photodetectors is not the limiting nonlinearity. Using the equations above, it is fairly straight forward to derive the *OIP*2 required of the receiver such that the *SFDR* for the entire photonic link is limited by third-order distortion due to the MZM over all bandwidths higher than 1 Hz as

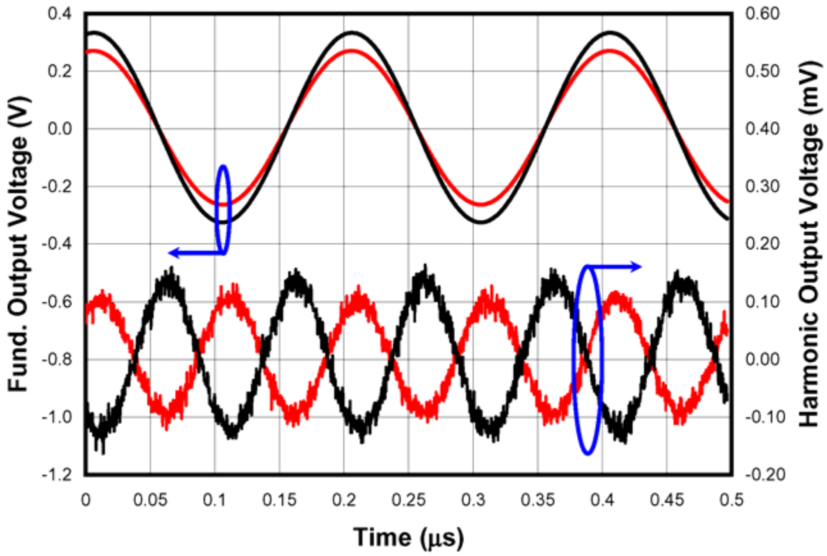

Fig. 4. Measured waveforms for the complementary outputs of the link. Shown are the fundamental (left axis) and second-harmonic (right axis) waveforms at the link output with one MZM arm (black) as compared to the other (red). The fundamentals are shown to be in phase, whereas the second harmonics are 180° out of phase. Because a different measurement setup was used for the fundamentals and the harmonics, nothing can be said about the relative phase of the fundamentals and harmonics.

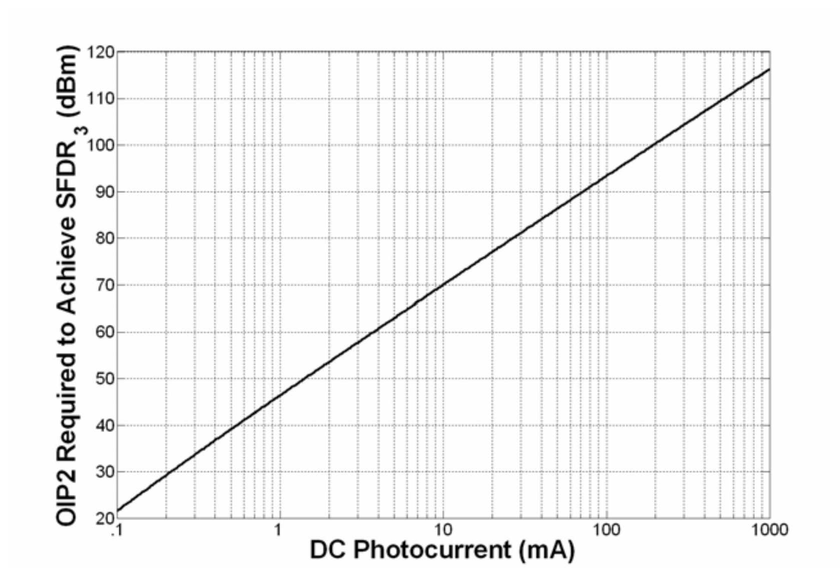

Fig. 5. Plot of the *OIP*2 required of a photodetector in order to achieve the *SFDR* performance afforded by the MZM in an analog-photonic link at a particular photocurrent.

$$OIP2_{\text{req,shot}} = \left(2I_{\text{dc}}\right)^{7/3}\left(\frac{1}{e}\right)^{1/3} Z_{\text{out}}\,, \tag{1.13}$$

where we have again assumed shot-noise-limited performance. A plot of Eq. (1.13) is shown in Fig. 5 as a function of I_{dc} with $Z_{\text{out}} = 50\ \Omega$. For the photonic link in consideration here we have I_{dc} = 26 mA, which puts the $OIP2$ required from the photodetectors at 80 dBm. With the measured

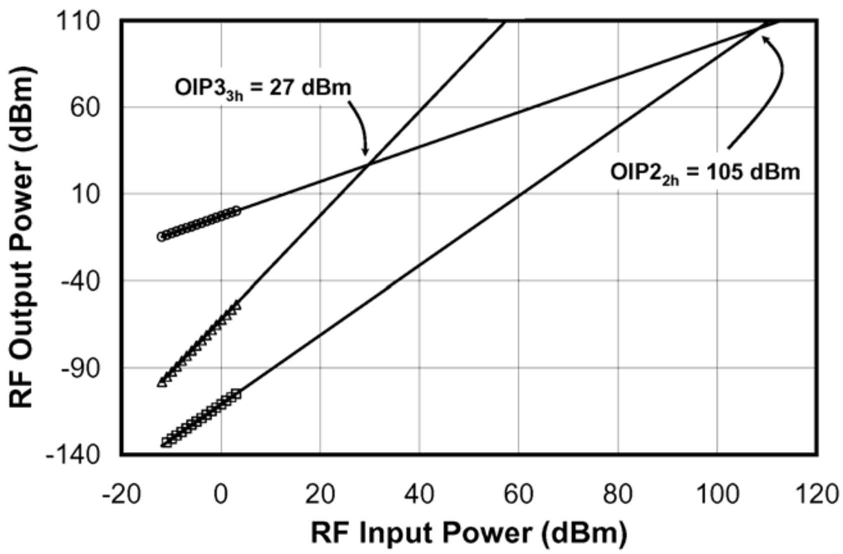

Fig. 6. The measured response for the entire link. The fundamental at 5 MHz is designated by circles, the third harmonic by triangles and the second harmonic by squares.

result of *OIP*2 = 105 dBm from Fig. 4 and applying the 6-dB correction to convert from harmonic to intermodulation distortion, we find that the 99-dBm *OIP*2 for the link is sufficient to remain third-order limited. Additional supporting data are provided in Fig. 6, where the measured fundamental response at 5 MHz along the associated second- and third-harmonic for the entire link is shown. The 105-dBm *OIP*2 is consistent with all of the above results and the 27-dBm *OIP*3 agrees well with $OIP3_{ph,3h}$ = 26.1 dBm predicted by Eq. (1.12) for I_{dc} = 26 mA and Z_{out} = 50 Ω.

Given the above results we can summarize the performance of the photonic link as G = –0.86 dB, NF = 21.0 dB, *OIP*2 = 99 dBm, and *OIP*3 = 21.3 dBm. Note here that the *OIP*2 is the minimum attainable *OIP*2 and a well-designed circuit to hold the MZM at quadrature is required to maintain that level. The resulting shot-noise-limited *SFDR* is 116.7 dB·Hz$^{2/3}$, which can be obtained from the above values or by using the shot-noise-limited equation for *SFDR*,

$$SFDR_{\rm shot} = \left(\frac{2I_{\rm dc}}{e}\right)^{2/3}, \tag{1.14}$$

with I_{dc} = 26 mA. The above metrics for the photonic link can then be employed to calculate the cascaded system performance with the RF front and back end as G = 30.1 dB, NF = 6.7 dB, $SFDR_2$ = 118.5 dB·Hz$^{1/2}$ and $SFDR_3$ = 109.9 dB·Hz$^{2/3}$. To improve on these metrics, a predistortion linearization technique can be used as described in [27]. A predistortion linearizer can be modeled as a black box placed before the MZM (see Fig. 2) with a particular gain and noise figure that has an infinite *OIP*3 and *OIP*2 but increases the *OIP*3 of the link without affecting the link's *OIP*2. The predistorter in [27] increased the link *OIP*3 by 8.9 dB and it is reasonable to assume that a predistorter can have unity gain with a 3-dB noise figure while maintaining that level of linearization. We can use these values to calculate the system performance with a linearized fiber-optic link as G = 30.1 dB, NF = 6.7 dB, $SFDR_2$ = 118.5 dB·Hz$^{1/2}$ and $SFDR_3$ = 111.2 dB·Hz$^{2/3}$. All of these results are summarized in Table 1. Compared to RF back-to-back, we see that the fiber-optic link incurs a 0.9-dB penalty in gain, a 1.1-dB penalty in noise figure, and a 1.7-dB penalty in $SFDR_3$, the limiting dynamic range metric. (The

Table 1

	G (dB)	NF (dB)	$SFDR_2$ (dB-Hz$^{1/2}$)	$SFDR_3$ (dB-Hz$^{2/3}$)
RF Back-toBack	31.0	5.6	120.7	111.6
w/ Optics	30.1	6.7	118.5	109.9
w/ Linearized Optics	30.1	6.7	118.5	111.2

compression dynamic range for a photonic link is derived in [16].) The *SFDR* of the system can be improved by applying a predistortion linearization to the photonic link, in which case the *SFDR* penalty by adding the photonic link to the system would be a mere 0.4 dB. Additional improvements may be possible, noting that the predistorter in [27] was designed to operate from 6-12 GHz and a better circuit can potentially be designed for HF.

3 FIBER EFFECTS

With RF performance metrics suitable for HF antenna remoting, the remaining justification for the use of photonics in HF applications lies in addressing the effects of the fiber-optic cabling itself. In this section we demonstrate that the link design described in Section 2 is not affected by the dominant fiber nonlinearities, chromatic dispersion and stimulated Brillouin scattering. These nonlinearities are discussed in Sections 3.1 and 3.2, respectively, and the treatments there are adaptations of work presented in [16], which should be referenced for a more-detailed description. We also show in Section 3.3 that the phase stability of a 7-km fiber-optic link is actually better than that for 300-m of traditional RF cabling.

3.1 Chromatic Dispersion

Photon-electron interactions in optical fiber give rise to a frequency-dependant index of refraction. A frequency-dependant index of refraction results in a frequency-dependant time delay for traversing a given length of fiber, commonly referred to as chromatic dispersion. The chromatic dispersion depends on the specific composition of the optical fiber and is quantified by the dispersion parameter D, which has units of $time \times wavelength^{-1} \times distance^{-1}$. Typically given in ps/(nm·km), D, a function of the optical wavelength, describes the time difference per nanometer wavelength difference for traversing a kilometer of fiber. The adverse effects that chromatic dispersion has on long-haul photonic systems are well understood [28]-[31] and the effects on an intensity-modulation direct-detection (IMDD) analog system have been examined [32]-[36]. Here, we state the equations that describe the adverse effect that chromatic dispersion has on an IMDD analog system and demonstrate that there is no incurred penalty for the link in Fig. 2.

The RF power response for an IMDD link, neglecting the frequency response of the MZM and photodiode(s), is given by

$$P_{\mathrm{rf}} = \frac{1}{2}\left(\frac{I_{\mathrm{dc}} V_{\mathrm{rf}} \pi}{V_{\pi}}\right)^2 Z_{\mathrm{out}} \cos^2\left(\frac{D L \lambda_{\mathrm{o}}^2 f_{\mathrm{rf}}^2 \pi}{c}\right), \tag{3.1}$$

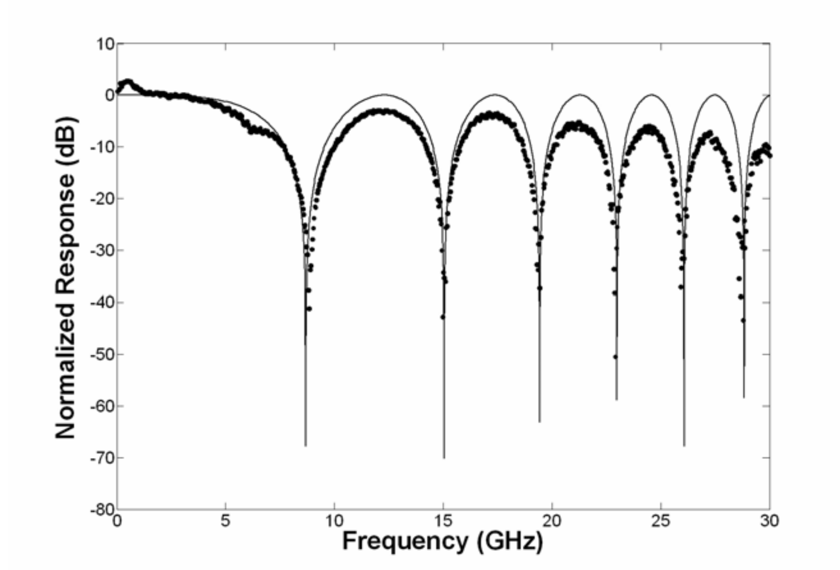

Fig. 7. The measured response (circles) for a 50-km IMDD link at 1551 nm with a dispersion parameter of 16.5 ps/(nm·km) shown against the response calculated using Eq. (3.1) with the same parameters.

where I_{dc} is the DC photocurrent, V_π is the MZM half-wave voltage, V_{rf} is the RF drive voltage, Z_{out} is the output impedance, L is the fiber length, λ_o is the optical wavelength, f_{rf} is the driving radio frequency, and c is speed of light in vacuum. We see that for $D = 0$, Eq. (3.1) dictates a flat response, which is expected. However, for $D \neq 0$ there is an RF-dependant power and P_{rf} can even be zero. Such periodic peaks and nulls in the RF response can be very problematic in wideband systems. This is demonstrated in Fig. 7 where measured data for an IMDD architecture are compared to those calculated using Eq. (3.1). Both the measured and calculated data are normalized to 0 dB and the experimental parameters $D = 16.5$ ps/(nm·km), $\lambda_o = 1551$ nm and $L = 50$ km are used. The measured and calculated data agree quite well, with the amplitude discrepancy at high frequencies being due to the frequency responses of the MZM and photodiode used in the experiment. The response shown in Fig. 7 would be quite unacceptable for a system operating over any octave above 4 GHz. In addition, we show in Fig. 8 the measured response for $L = 50$ km and $L = 100$ km, both with the same λ_o and D, showing that the useable RF bandwidth decreases significantly for longer distances. In addition to Eq. (3.1), it is useful to calculate the k^{th}-order null in radio frequency, fiber length, or delay time as

$$f_{\mathrm{rf,null}}(\mathrm{GHz}) = 3.87 \times 10^5 \left(\frac{1+2k}{D\left(\frac{\mathrm{ps}}{\mathrm{nm}\cdot\mathrm{km}}\right) L(\mathrm{km}) \lambda_o^2(\mathrm{nm})} \right)^{1/2} \tag{3.2}$$

$$L_{\mathrm{null}}(\mathrm{km}) = 1.50 \times 10^{11} \left(\frac{1+2k}{D\left(\frac{\mathrm{ps}}{\mathrm{nm}\cdot\mathrm{km}}\right) f_{\mathrm{rf}}^2(\mathrm{GHz}) \lambda_o^2(\mathrm{nm})} \right) \tag{3.3}$$

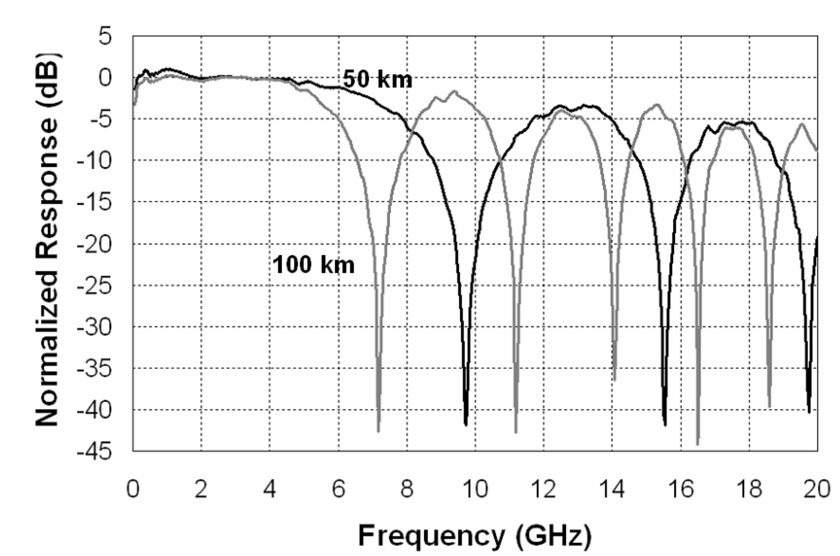

Fig. 8. The measured response for an IMDD link with L = 50 km (black) and L = 100 km (grey), with both links operating at the same optical wavelength and having the same dispersion parameter.

$$t_{\mathrm{null}}(\mu\mathrm{s}) = 7.34\times10^{11}\left(\frac{1+2k}{D\left(\frac{\mathrm{ps}}{\mathrm{nm}\cdot\mathrm{km}}\right) f_{\mathrm{rf}}^{2}(\mathrm{GHz})\lambda_{\mathrm{o}}^{2}(\mathrm{nm})}\right), \tag{3.4}$$

where k = 0, 1, 2… and we have explicitly shown the units to facilitate easy calculations. Equations (3.1)-(3.4) demonstrate that significant power penalties can occur as a result of chromatic dispersion. Other detrimental effects not discussed here include the increase of even-order distortions [34] and the enhancement of multichannel fiber nonlinearities such as self-phase modulation and cross-phase modulation [34],[37],[38]. In addition, chromatic dispersion imposes similar limitations on all analog modulation formats, as has been demonstrated for polarization and phase modulation [35],[39],[40]. It is therefore essential to consider chromatic dispersion compensation for any high-performance analog link with a length greater than a few kilometers.

Figures 7 and 8 seem to suggest that there is no appreciable penalty due to chromatic dispersion in the HF range, even at transmission distances upwards of 100 km. To demonstrate this point more clearly, we employ Eq. (3.1) to calculate the normalized response at 30 MHz as a function of transmission distance. (Being the highest frequency in the HF band, the penalty will be worst at 30 MHz.) The results of this calculation are shown in Fig. 9 and demonstrate clearly that the chromatic dispersion will not affect the HF system of interest. For a transmission distance of 7 km there is approximately a -3×10^{-11} dB penalty in the fundamental at 30 MHz, a value that is not measurable with standard RF equipment. Even at a distance of 10,000 km, which is roughly one-fourth of Earth's circumference [41], the penalty is a mere -6×10^{-5} dB. Finally, we can calculate the length at which the first null occurs as 4.2 million km, where we have used k = 0, D = 16.5 ps/(nm·km), f_{rf} = 30 MHz and λ_{o} = 1551 nm in Eq. (3.3). All of these calculations, based on well-established theory, explicitly show that chromatic dispersion is not an issue for HF antenna remoting using fiber optics.

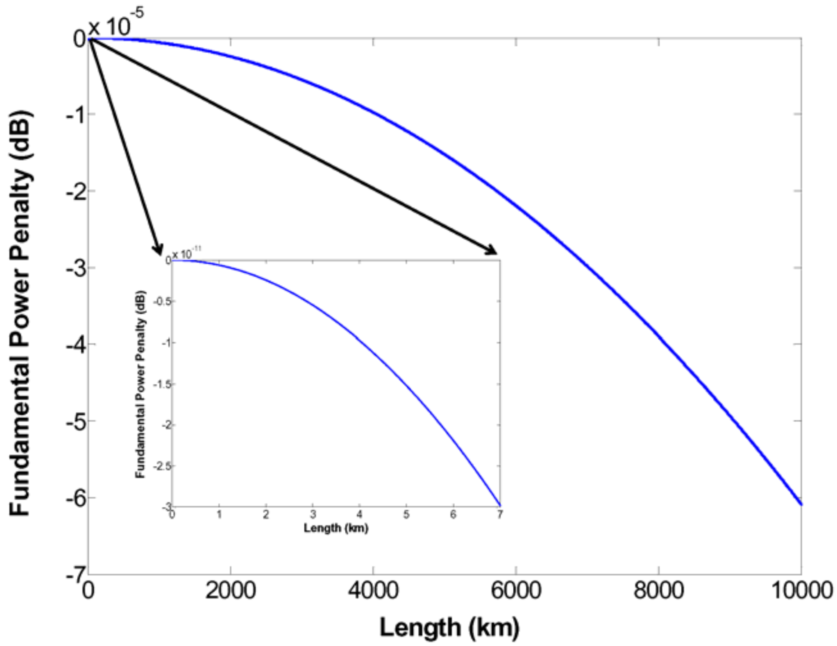

Fig. 9. The calculated power penalty due to chromatic dispersion for a 30-MHz fundamental as a function of transmission distance. The inset shows the penalty out to 7 km, the remoting distance of interest for this report.

3.2 Stimulated Brillouin Scattering

In a long-haul architecture, the amount of optical power that can be linearly transmitted through a length of fiber is limited by Brillouin scattering. Brillouin scattering in a crystal occurs when a photon is annihilated with the subsequent emission of 1) a lower-frequency photon and a phonon (Stokes process) or 2) a higher-frequency photon (anti-Stokes process) [42]. Brillouin scattering in fiber-optic cabling can be stimulated, particularly via the Stokes process in the direction counter to the pump [28]. This stimulated Brillouin scattering (SBS) in fiber is well-understood and documented elsewhere [43],[28],[44]. It is our intention here to describe the detrimental effects that SBS has on a long-haul analog architecture using experimental data.

The fundamental problem posed by SBS in a fiber-optic system is depicted in Fig. 10. Shown in Fig. 10 are measured data for the optical-power response of a 20-km section of SMF-28. At low input powers, the optical output power is linearly related to the input power and offset by the optical power loss, approximately 6 dB in this case. In this regime, there is also power that is back-scattered to the input of link, which is about 15-dB down from the input power. This linearly-backscattered power is due to various scattering processed including elastic Rayleigh scattering, inelastic Raman scattering and inelastic Brillouin scattering [28]. The latter two processes differ in that Raman scattering involves optical phonons, whereas Brillouin scattering involves acoustic phonons. We see that around 7-dBm input power, the backscattered power increases dramatically whereas the optical output power saturates. This threshold is due to the onset of SBS. From the data in Fig. 10, it is clearly seen that SBS limits the amount of optical power that can be transmitted through a length of fiber. In addition, it is typically the case for optical fiber that the backscattered optical power spectrum is downshifted in frequency by a value near 10 GHz, corresponding to the Stokes frequency for the fiber. Once the backscattered power is high enough, a significant portion will elastically scatter in the forward-propagating direction, resulting in a spurious tone in the electrical domain. This spur is a result of the "mixing" of the pump signal and the SBS wave, therefore occurring at the Stokes frequency. Such a spurious

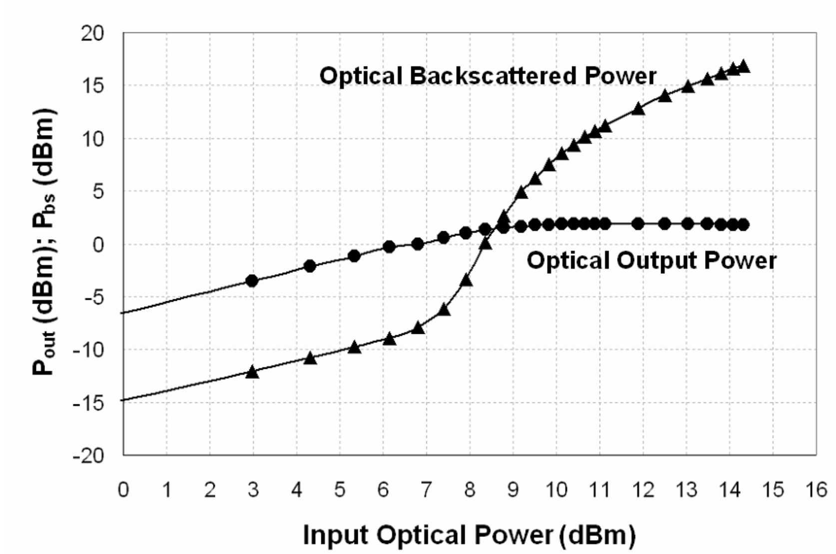

Fig. 10. The measured optical power response for 20-km of SMF-28. Shown are the optical output power at the end of the fiber span (circles) and the optical power scattered back to the fiber span input (triangles) as a function of optical input power. Here, the optical pump is a 1551-nm semiconductor distributed feedback laser with a linewidth of about 1 MHz.

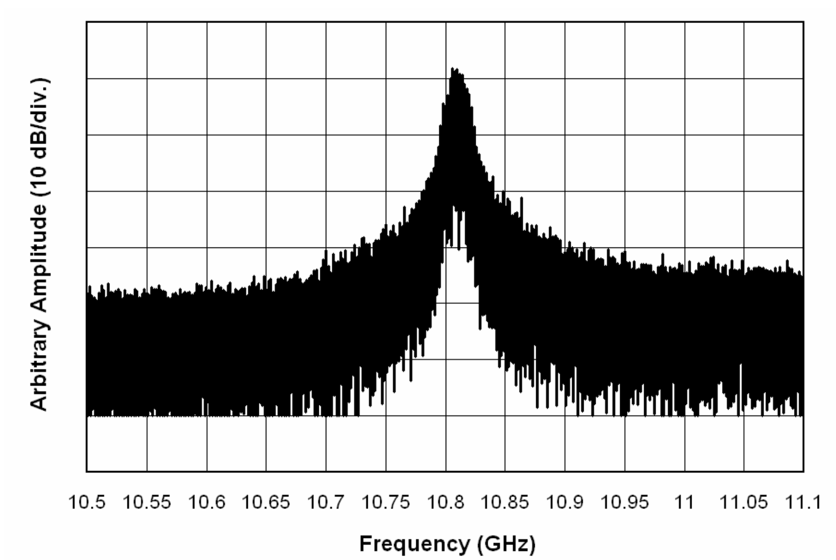

Fig. 11. Measured noise in the electrical domain for a 20-km span of SMF-28 fiber with a 1551-nm pump at a linewidth of about 1 MHz. The pump is operated beyond the measured SBS threshold of 7 dBm (see Fig. 10).

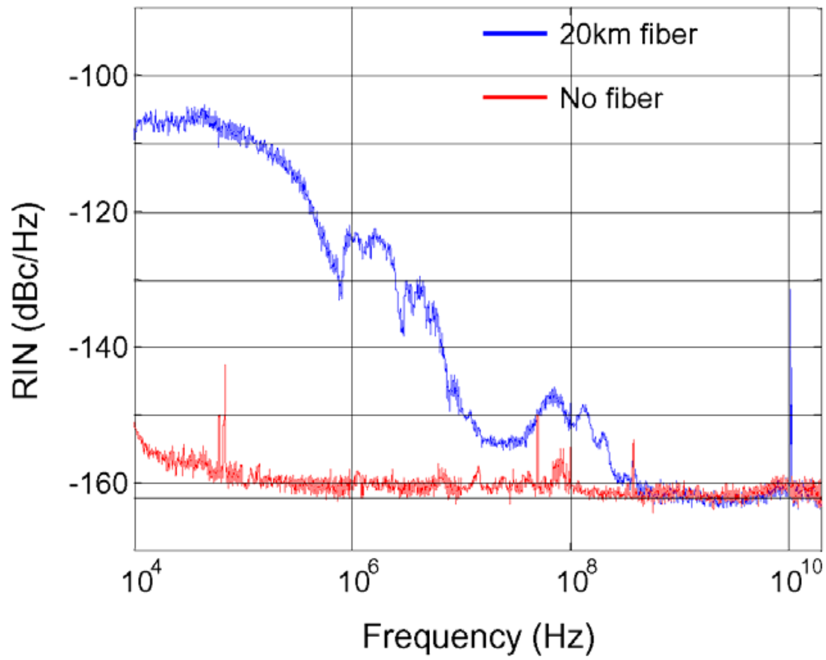

Fig. 12. The measured electrical noise for a 20-km custom span of fiber operating 3.5 dB beyond the SBS threshold (blue) compared to the noise of the laser-photodiode combination only (red). The pump is a distributed feedback semiconductor laser with a linewidth on the order of 300 kHz. All of the excess noise at low frequency is attributed to the SBS process. Note the peaks near 10 GHz, consistent with the Stokes frequencies for the custom fiber span.

tone has a line shape due to a convolution of the phonon spectrum for the fiber with the laser line shape. Shown in Fig. 11 are measured data for the noise in the electrical domain due to SBS. The parameters for this measurement are the same as in Fig. 10 at an optical input power beyond the 7-dBm SBS threshold. Under these conditions, we observe a peak in the noise at about 10.82 GHz. It is worth noting that this peak frequency and the structure around the peak are a function of the pump properties and the properties of the fiber itself. We also note that in addition to the significant noise near the Stokes frequency, it has been reported in [45] that noise at low electrical frequencies has also been observed in systems operating beyond the SBS threshold. We have since quantified this result and have measured as much as a 40-dB increase in the noise at 1 MHz when operating beyond the SBS threshold. A representative spectrum is shown in Fig. 12 demonstrating the need to operate below the SBS threshold for HF applications. As a qualitative summary, we list the detrimental effects of SBS as 1) limitation of the amount of optical power that can be transmitted through a fiber span, 2) significant electrical noise at the Stokes frequency and 3) increased electrical noise at low frequency.

The analytical analysis of the detrimental effects of SBS starts with the equation for the SBS threshold [46],

$$P_{\mathrm{th}} \approx \frac{21 A_{\mathrm{eff}}}{L_{\mathrm{eff}} g_{\mathrm{B}}}, \tag{3.5}$$

where A_{eff} is the affective area of the fiber, L_{eff} is the effective length of the fiber and g_{B} is the Brillouin gain coefficient. We can write the effective length as [46]

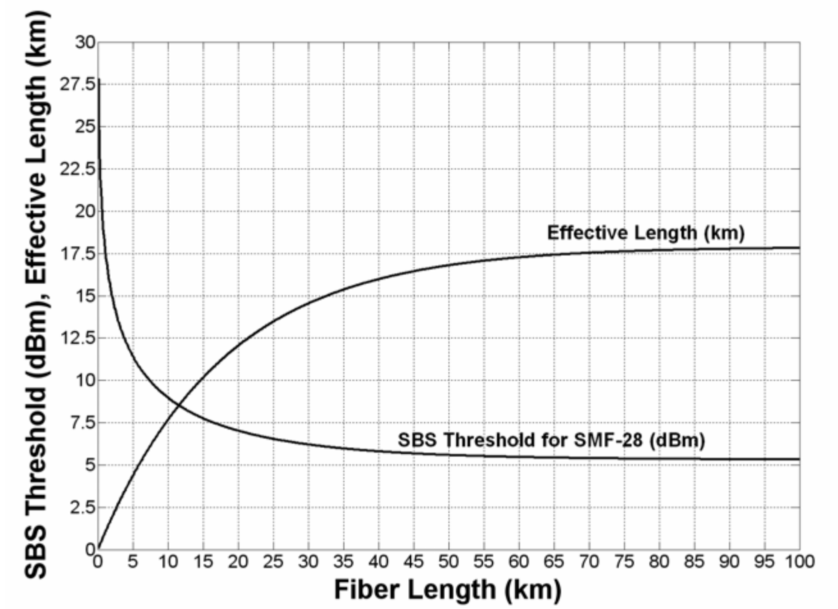

Fig. 13. Calculated SBS threshold and effective length for SMF-28 with a 1551-nm pump at 1-MHz linewidth. These data were calculated using the measured data point P_{th} = 7 dBm for L = 20 km and α = 0.94/km with Eqs. (3.5) and (3.6).

$$L_{\text{eff}} = \frac{1-e^{-\alpha L}}{\alpha}, \tag{3.6}$$

where α is the fiber loss and L is the physical length. For most fiber types, $\alpha \sim 0.94$/km (0.25 dB/km) and Eq. (3.6) can be generally determined. However, A_{eff} and g_{B} are not easily obtained and Eq. (3.5) is not always practical to calculate. We always have the conditions that $P_{\text{th}} \propto L_{\text{eff}}^{-1}$ and A_{eff} and g_{B} are not functions of L, which allows us to calculate P_{th} as a function of L, given that we know α and P_{th} for a particular fiber at one L. We carry out this calculation for SMF-28 where we use the data in Fig. 4.2.1, P_{th} = 7 dBm for L = 20 km. The results of this calculation are shown in Fig. 13. The SBS threshold and effective length are plotted as a function of physical fiber length in Fig. 13, demonstrating that the effective length dominates all other terms in Eq. (3.5) as $L \to \infty$. Figure 13 demonstrates the utility of data sets such as shown in Fig. 10 and we stress that an experimental characterization of a particular fiber run is the best way to analyze the effects of SBS.

From the data in Fig. 13, we can say that the SBS threshold for 7 km of SMF-28 is slightly greater than 10 dBm and the preceding experimental data dictates that SBS must be mitigated for a high-performance HF link. There exists a host of methods employed to combat the problems posed by SBS in lightwave systems. Applying temperature [47] or strain [48] distributions to the fiber have been reported as SBS-mitigation techniques. While such methods work in principle, they are difficult to implement in a real system. Because the SBS threshold is inversely proportional to the linewidth of the transmitter [28], SBS suppression has been demonstrated by artificially broadening the signal source [49]. This "dithering" technique is acceptable for digital systems, but can cause additional distortions in a high-fidelity analog architecture. A very useful passive technique to mitigate SBS is to construct a fiber span from sections of fibers that have different SBS frequencies [50]-[53]. Such an alternating-fiber technique is very effective in analog optical delay lines [44],[54] but splicing together multiple spans of different fiber types is not practical for a deployed antenna-remoting system. The development above explains explicitly then why we employ four fibers in link design presented in Section 2. With the given laser and MZM for the link, four fibers allows for the transmission of all available laser power without any detrimental effects due to SBS. This mitigation technique is completely passive and scalable in the sense that additional fibers can be added to a bundle of fiber (with a minimal increase in cost) to increase the optical power handling of the link. For example, in this 7-km example the effective SBS threshold is 10 dBm + 10log(N), where N is the fiber count. Increasing N beyond four in this application provides no added benefit because of limited laser power on the transmit side. The only downside to this method is that each fiber must be phase matched but as we will see in the next subsection, phase stability for fiber-optic cabling in the HF range is quite good.

3.3 Phase Stability

In previous sections we have presented a fiber-optic link design that includes four fibers per link. Two fibers are required in order to cancel common-mode noise at the MZM input and linearization of photodiode-limited even-order distortion; additional fibers increase the optical power handling of the link limited by SBS and minimize the photocurrent on each individual photodiode. With all of these afforded advantages, the one disadvantage is that the fibers must be phase matched. Phase matching a fiber at 30 MHz, where the wavelength is about 10 m, is practically trivial. The difficulty lies in maintaining phase match over long distances in the environment. This obstacle can be overcome by employing active stabilization techniques, as is often done to very high precision for very high frequencies [9],[55]-[59]. However, we will show in this section that cables can remain phase matched in the HF range without any additional active components.

The dominant mechanisms that dictate the phase stability of a fiber-optic transmission line are strain and temperature [60]. Strain-induced effects are particularly important for fiber-optic cabling comprised of bundles of individual fibers, but it has been shown that cables are available that are robust against these detriments [60]. Here, we consider phase changes caused by temperature differences for individual fibers separated in the field and in a fiber bundle with a temperature gradient across it. The governing relationship used for the analysis is

$$t = \frac{nL}{c}, \tag{3.7}$$

which describes the time t it takes a signal to traverse a given length of fiber L, where n = 1.468 is the index of refraction and c is the speed of light in vacuum. (We addressed first-order chromatic dispersion in Section 3.1.) We use the chain rule to obtain the derivative of Eq. (3.7) with respect to temperature and convert time to RF phase yielding

$$\frac{d\phi}{dT} = \frac{360 f_{\text{rf}}}{c}\left(L\frac{dn}{dT} + n\frac{dL}{dT}\right), \tag{3.8}$$

where f_{rf} is the signal radio frequency, $dn/dT = 1.2\times10^{-5}/^\circ C$ is the temperature dependence of the index of refraction, and $dL/dT = L\cdot TEC$ where $TEC = 5.6\times10^{-7}/^\circ C$ is the thermal expansion coefficient for the fiber. We have obtained the values for dn/dT and dL/dT from [61]. In Figure 14, $\Delta\phi$ is plotted as a function of ΔT for f_{rf} = 12 GHz and L = 20 m, showing close agreement between measured data and the calculation given by Eq. (3.8). We therefore can employ Eq. (3.8) to analyze the relative phase change between fibers at different temperatures.

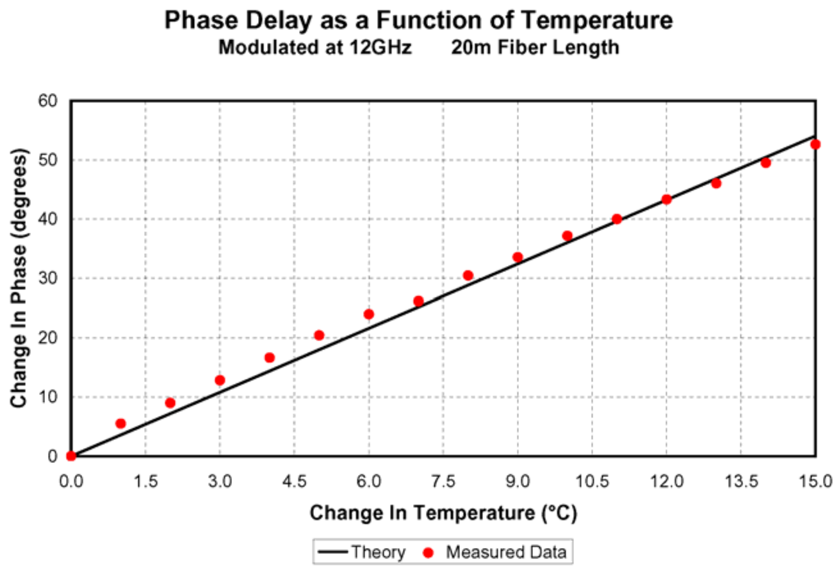

Fig. 14. The phase drift in a single 20-m fiber modulated at 12 GHz as a function of temperature. The theory is according to Eq. (3.8).

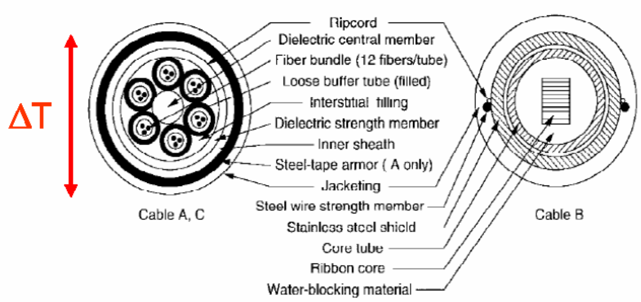

Cable	Diameter (cm)	Minimum Bend Radius (cm)	Spiral Period (cm)	Fiber Count
A	1.4	15	10	6 tubes (12 SMFs/tube)
B	1.8	18	90	18 ribbons (12 SMFs/ribbon)
C	1.2	15	10	6 tubes (12 SMFs/tube)

Fig. 15. Taken from [60]. The schematic for three fiber-optic cables used in the phase-stability analysis.

In addition to Eq. (3.8), we can use the results from [60] to analyze the phase performance of a fiber-optic cable comprising numerous co-located fibers. According to [60], three different fiber optic cables (see Fig. 15) with L = 5 m and a temperature gradient $\Delta T \leq 40$°C in the transverse dimension were observed to have a phase change $\Delta\phi \leq 1°$ for f_{rf} = 18 GHz. These values in Eq. (3.8) predict a phase change of 55.5°, with the difference due to the fact that the fibers are co-located and the temperature difference is across the transverse dimension of the cable. Any temperature change along the axial dimension will be common to all fibers and we can use a "1/55 insulation factor" for Eq. (3.8) in predicting the phase stability of a fiber cable with up to 216 individual fibers (see Fig. 15).

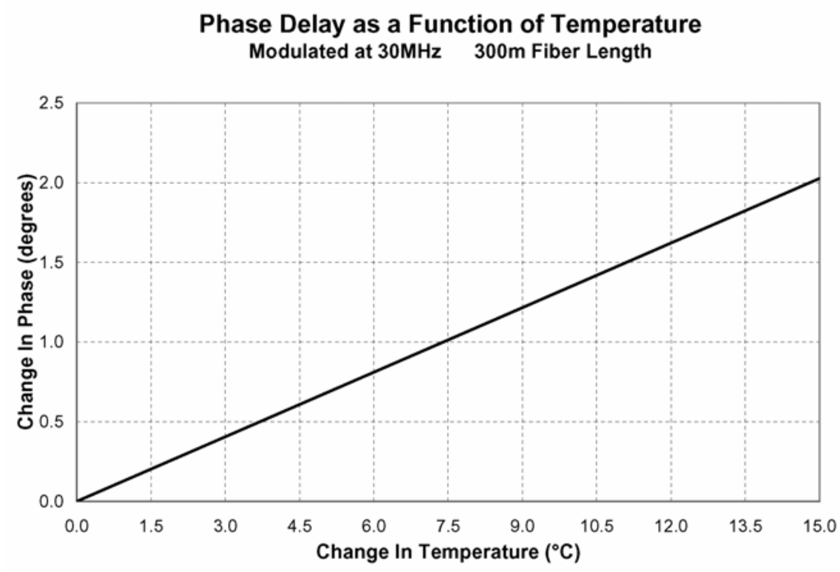

Fig. 16. The calculated phase drift in a single 300-m fiber modulated at 30 MHz as a function of temperature. The result is obtained from Eq. (3.8) and the slope is 0.14°/°C.

With the above results we can analyze the phase stability of a fiber-optic HF system such as that shown in Fig. 1. We carry out the analysis at f_{rf} = 30 MHz because any phase variations will be worst at the top of the HF band. First, we calculate the maximum phase error in the fiber-optic trunk as $\Delta\phi = 0.6°$ for a $\Delta T \leq 10°C$ and L = 6.7 km using Eq. (3.8) with the insulation factor. A 10°C temperature gradient along the transverse direction (< 2 cm) is quite extreme and in reality we expect no phase error at 30 MHz due to the fiber-optic cable. If an appreciable temperature gradient does exist, burying the fiber provides a shielding factor given by $\exp(-\text{depth}/7.4\ \text{cm})$ [62]. For example, if the fiber is buried 0.5 m there is a 1.2×10^{-3} reduction in the temperature swing relative to the surface. The major source of phase error will be due to the exposed fiber linking each antenna element to the fiber trunk. We assume that the radius of the CDAA is at most L = 300 m and use Eq. (3.8) to calculate the relative phase change as 0.14°/°C at 30 MHz (see Fig. 16). To put this result in perspective, the phase change for LMR-600 RF cabling under the same conditions is 0.21°/°C. Therefore, a fiber-optic link such as that shown in Fig. 1 with a 300-m array radius and a 6.7-km fiber cable run will be more robust to phase change due to temperature change than 300 m of LMR-600 RF cabling.

Table 2

	G (dB)	NF (dB)	SFDR (dB-Hz$^{2/3}$)	Length (m)	Phase Slope (deg/deg C)
RF Back-to-Back	31.0	5.6	111.6	n/a	n/a
RF Link	26.8	5.7	114.3	300	0.21
Optics Only	-0.86	21	116.7	7000	0.14
Optical Link	30.1	6.7	109.9	7000	0.14
Optical vs. RF Link	3.3	1.0	-4.4	14 dB	-0.07

4 SUMMARY AND CONCLUSIONS

The results of this analysis are summarized in Table 2. The RF back-to-back performance includes an RF preamplifier and an ADC. The RF link performance includes 300 m of LMR-600 between the preamplifier and the ADC. The optical link performance is given by replacing the LMR-600 with 7 km of fiber. While a fair comparison is certainly on a case-by-case basis and depends on the RF front and back end, we believe this analysis to be representative of what to expect in the field. This being said, the most important result of this work is given in Row 3 of Table 2, the performance of the optical link itself. These performance metrics along with analysis in Section 2 allow for the predicted performance with any RF system. These results hold across the 2-30 MHz band in the laboratory and slight deviations may occur in the field depending on the environmental noise. However, we have taken into account environmental effects on the phase stability as described in Section 3.3. We have also addressed any other fiber nonlinearities for a single-optical-channel link. While the design and analysis of the fiber-optic link presented here are unique, we note that the components required to implement the design are commercial-off-the-shelf parts.

The link design presented here is suitable and adequate for HF antenna-remoting applications. In the case that improved performance is demanded for next-generation systems, the following research can be undertaken. First, a multi-octave predistortion linearization technique can most likely be implemented for an HF photonic link. This would improve the third-order spurious-free dynamic range and the difficulties lie in not introducing even-order distortion in the process. Presently, such a predistorter does not exist. The novel technique of suppressing photodiode-induced even-order distortion in this link can also be expanded. Single- and arrayed-photodiode research is ongoing and non-commercial detectors are required for significantly increased performance. Increasing the optical power handling of the detectors necessitates a high-power front end and increased power handling of the fiber, requiring research in low-noise high-power optical amplifiers and fiber nonlinearity mitigation. The remoting distance could be extended to much longer distances utilizing novel modulations formats in addition to the above-mentioned research. Next-generation goals include a 100-km stand-off from the array. Other expanded-scope possibilities in HF photonics include a two-way optical link where the up-link could be used to calibrate the array.

HF analog photonics is an enabling technology for antenna-remoting and direction-finding applications. As detailed in this report, the technology for acceptable performance is available today. The analysis in this report, carried out using well-established theory, leaves little question as to the viability of HF antenna remoting with fiber optics. Previous results in fields such as radio astronomy and telecommunications also demonstrate the utility of fiber optics. While we have provided substantial experimental results, field trials are ultimately required to validate the performance but should be completed in the near future. Subsequent upgrades and expanded-scope capabilities are also possible for the fiber-optic link presented here, strongly noting that the present performance is suitable for many of today's applications.

REFERENCES

[1] R. C. Benoit and M. W. Furlow, “Wullenweber type ultra high frequency radio direction finder,” *IRE Intl. Convention Record*, Part 5, p. 109, 1955.

[2] R. C. Benoit and M. W. Furlow, “Design for wide-aperture direction finders,” *TeleTech & Electronics Industries*, p. 60, Sept. 1955.

[3] E. Hudock, “High frequency steerable bean antenna system,” *IRE Intl. Convention Record*, vol. 5, Part 1, pp. 78-86, Mar. 1957.

[4] W. H. Kummer, “Broad-band microwave electronically scanned direction finder,” *IEEE Trans. Antennas and Propagation*, vol. AP-31, no. 1, pp. 18-26, Jan. 1983.

[5] W. R. Vincent and R. W. Adler, “Performance comparison AN/FRD-10 vs. PUSHER,” Naval Postgraduate School Technical Report, AD-A283263, Feb. 1994.

[6] T. D. Gehrki, “An analysis on the effects of feedline and ground screen noise currents on a conical monopole receiving antenna,” Naval Postgraduate School Technical Report, AD-A283401, June 1994.

[7] R. Spencer, L. Hu, B. Smith, M. Bentley, I. Morison, B. Anderson, D. Moodie, M. Robertson, and D. Nesset, “The use of optical fibers in radio astronomy,” *J. Mod. Optics*, vol. 47, no. 11, pp. 2015-2020, 2000.

[8] P. R. Jewell and R. M. Prestage, “The Green Bank Telescope,” *Proc. of SPIE*, vol. 5489, pp. 312-323, 2004.

[9] S. Montebugnoli, M. Boschi, F. Perini, P. Faccin, G. Brunori, and E. Pirazzini, “Large antenna array remoting using radio-over-fiber techniques for radio astronomical application,” *Microwave and Opt. Technol. Lett.*, vol. 46, no. 1, pp. 48-54, July 2005.

[10]K. J. Williams, L. T. Nichols, and R. D. Esman, “Externally-modulated 3 GHz fibre optic link utilizing high current and balanced detection,” *Electron. Lett.*, vol. 33, no. 15, pp. 1327-1328, July 1997.

[11]D. M. Pozar, “Microwave Engineering,” 2nd ed., Wiley: New York, 1998.

[12]P. B. Kenington, “Highly Linear RF Amplifier Design,” Artech, 2000.

[13]S. A. Maas, “Third-order intermodulation distortion in cascaded stages,” *IEEE Microwave and Guided Wave Lett.*, vol. 5, no. 6, pp. 189-191, June 1995.

[14]G. P. Agrawal, Fiber-Optic Communications Systems, Wiley, New York, 1997.

[15]J. D. McKinney, M. Godinez, V. J. Urick, S. Thaniyavarn, W. Charczenko, and K. J. Williams, “Sub-10-dB noise figure in a multiple-GHz analog optical link,” *IEEE Photon. Technol. Lett.*, vol. 19, no. 7, pp. 465-467, Apr. 2007.

[16]V. J. Urick, “Long-haul analog photonics principles with applications,” Doctoral Dissertation, UMI No. 3255815, May 2007.

[17]J. Geist and H. Baltes, “High accuracy modeling of photodiode quantum efficiency,” *Appl. Opt.*, vol. 28, no. 18, pp. 3929-3939, Sept. 1989.

[18]R. R. Hayes and D. L. Persechini, “Nonlinearity of p-i-n photodetectors,” IEEE Photon. Technol. Lettt., vol. 5, no. 1, pp. 70-72, Jan. 1993.

[19]K. J. Williams, “Nonlinear mechanisms in microwave photodetectors operated with high intrinsic region electric fields,” *Appl. Phys. Lett.*, vol. 65, no. 10, pp. 1219-1221, Sept. 1994.

[20]K. J. Williams, R. D. Esman, and M. Dagenais, “Nonlinearities in p-i-n microwave photodetectors,” *J. Lightwave Technol.*, vol. 14, no. 1, pp. 84-96, Jan. 1996.

[21]Y. Kuhara, Y. Fujimura, N. Nishsyama, H. Terauchi, and N. Yamabayashi, “Characterization and theoretical analysis of second-order intermodulation distortion of InGaAs/InP p-i-n photodiode modules for fiber-optic CATV,” *J. Lightwave Technol.*, vol. 15, no. 4, pp. 636-641, Apr. 1997.

[22]K. J. Williams and R. D. Esman, “Photodiode DC and microwave nonlinearity at high currents due to carrier recombination nonlinearities,” *IEEE Photon. Technol. Lett.*, vol. 10, no. 7, pp. 1015-1017, July 1998.

[23]H. Jiang and P. K. L. Yu, "Equivalent circuit analysis of harmonic distortion in photodiodes," *IEEE Photon. Technol. Lett.*, vol. 10, no. 11, pp. 1608-1610, Nov. 1998.
[24]K. J. Williams and R. D. Esman, "Design considerations for high-current photodetectors," *J. Lightwave Technol., vol. 17, no. 8, pp. 1443-1454*, Aug. 1999.
[25]H. Jiang, D. S. Shin, G. L. Li, T. A. Vang, D. C. Scott, and P. K. L. Yu, "The frequency behavior of the third-order intercept point in a waveguide photodiode," *IEEE Photon. Technol. Lett.*, vol. 12, no. 5, pp. 540-542, May 2000.
[26]T. H. Stievater and K. J. Williams, "Thermally induced nonlinearities in high-speed p-i-n photodetectors," *IEEE Photon. Technol. Lett.*, vol. 16, no. 1, pp. 239-241, Jan. 2004.
[27]V. J. Urick, M. S. Rogge, P. F. Knapp, L. Swingen, and F. Bucholtz, "Wideband predistortion linearization for externally-modulated long-haul analog fiber optic-links," *IEEE Trans. Microwave Theory Tech.*, vol. 54, no. 4, pp. 1458-1463, Apr. 2006.
[28]G. P. Agrawal, "Nonlinear fiber optics," 3rd ed., San Diego: Academic Press, 2001.
[29]J. Wang and K. Peterman, "Small signal analysis for dispersive optical fiber communication systems," *J. Lightwave Technol.*, vol. 10, no. 1, pp. 96-100, Jan. 1992.
[30]J. Wang and J. M. Kahn, "Impact of chromatic dispersion and polarization-mode dispersions on DPSK systems using interferometric demodulation and direct detection," *J. Lightwave Technol.*, vol. 22, no. 2, pp. 362-371, Feb. 2004.
[31]A. Bononi and A. Orlandini, "Small-signal analysis of amplitude-, phase-, and polarization-to-intensity conversion in general optical linear systems with application to PMD compensation," *J. Lightwave Technol.*, vol. 23, no. 3, pp. 1074-1082, Mar. 2005.
[32]H. Schmuck, "Comparison of optical millimeter-wave system concepts with regard to chromatic dispersion," *Electron. Lett.*, vol. 31, no. 21, pp. 1848-1849, Oct. 1995.
[33]J. L. Corral, J. Marti, and J. M. Fuster, "General expression for IM/DD dispersive analog optical links with external modulation or optical up-conversion in a Mach-Zehnder electrooptical modulator," *IEEE Trans. Microwave Theory Tech.*, vol. 49, no. 10, pp. 1968-1976, Oct. 2001.
[34]E. E. Funk, A. L. Campillo, and D. A. Tulchinsky, "Nonlinear distortion and crosstalk in microwave fiber-radio links," in *IEEE MTT-S Digest*, vol. 3, pp. 1691-1693, June 2002.
[35]V. J. Urick and F. Bucholtz, "Compensation of arbitrary chromatic dispersion in analog links using a modulation-diversity receiver," *IEEE Photon. Technol. Lett.*, vol. 17, no. 4, pp. 893-895, Apr. 2005.
[36]J. D. McKinney and J. Diehl, "Measurement of chromatic dispersion using the baseband radio-frequency response of a phase-modulated analog optical link employing a reference fiber," NRL Memorandum Report, NRL/MR/5652-07-9072, Sept. 2007.
[37]F. Bucholtz, V. J. Urick, and A. L. Campillo, "Comparison of crosstalk for amplitude and phase modulation in an analog fiber optic link," in *IEEE Microwave Photonics Technical Digest*, Ogunquit, pp. 66-69, Oct. 2004.
[38]M. S. Rogge, V. J. Urick, F. Bucholtz, K. J. Williams, and P. Knapp, "Comparison of amplitude and phase modulation crosstalk in hyperfine WDM fiber optic links," in *CLEO Technical Digest*, Baltimore, paper CMH2, May 2005.
[39]A. L. Campillo, F. Bucholtz, and K. J. Williams, "Dispersion impairments in analog polarization modulated links," in *Microwave Photonics Technical Digest*, Ogunquit, pp. 104-106, Oct. 2004.
[40]A. L. Campillo and F. Bucholtz, "Chromatic dispersion effects in analog polarization-modulated links," *Appl. Opt.*, vol. 45, no. 12, pp. 2742-2748, Apr. 2006.
[41]http://www.nasa.gov/worldbook/earth_worldbook.html
[42]C. Kittel, "Introduction to solid state physics," 7th ed., New York: Wiley, 1996.
[43]R. G. Smith, "Optical power handling capacity of low loss optical fibers as determined by stimulated Raman and Brillouin scattering," *Appl. Opt.*, vol. 11, no. 11, pp. 2489-2494, Nov. 1972.

[44]A. L. Campillo, F. Bucholtz, and K. J. Williams, "Maximizing optical power throughput in long fiber optic links," NRL Memorandum Report, NRL/MR/5650-06-8946, Apr. 2006.
[45]J. Zhang and M. R. Phillips, "Modeling intensity noise caused by stimulated Brillouin scattering in optical fibers," *Conference on Lasers and Electro-Optics Digest*, paper CMH6, pp. 140-142, May 2005.
[46] G. P. Agrawal, Fiber-Optic Communications Systems, 2nd edition, John Wiley & Sons, New York, 1997.
[47]J. Hansryd, F. Dross, M. Westlund, P. A. Andrekson, and S. N. Knudsen, "Increase of the SBS threshold in a short highly nonlinear fiber by applying a temperature distribution," *J. Lightwave Technol.*, vol. 19, no. 11, pp. 1691-1697, Nov. 2001.
[48]J. M. C. Boggio, J. D. Marconi, and H. L. Fragnito, "Experimental and numerical investigation of the SBS-threshold increase in an optical fiber by applying strain distributions," *J. Lightwave Technol.*, vol. 23, no. 11, pp. 3808-3814, Nov. 2005.
[49]G. C. Wilson, T. H. Wood, J. L. Zyskind, J. W. Sulhoff, J. E. Johnson, T. Tanbun-Ek, and P. A. Morton, "SBS and MPI suppression in analogue systems with integrated electroabsorption modulator/DFB laser transmitters," *Electron. Lett.*, vol. 32 no. 16, pp. 1502-1504, Aug. 1996.
[50]X. P. Mao, R. W. Tkach, A. R. Chraplyvy, R. M. Jopson, and R. M. Derosier, "Stimulated Brillouin threshold dependence on fiber type and uniformity," *IEEE Photonics Technol. Lett.*, vol. 4, no. 1, pp. 66-69, Jan. 1992.
[51]C. A. S. de Oliveira, C. K. Jen, A. Shang, and C. Saravanos, "Stimulated Brillouin scattering in cascade fibers of different Brillouin frequency shifts," *J. Opt. Soc. Am. B*, vol. 10, no. 6, pp. 969-972, June 1993.
[52]S. Rae, I. Bennion, and M. J. Cardwell, "New numerical model of stimulated Brillouin scattering in optical fibers with nonuniformity," *Optics Communications*, vol. 123, pp. 611-616, Feb. 1996.
[53]A. Kobyakov, M. Sauer, and J. E. Hurley, "SBS threshold of segmented fibers," in *OFC Technical Digest*, Anaheim, paper OME5, Mar. 2005.
[54]V. J. Urick, P. F. Knapp, L. Swingen, M. S. Rogge, A. L. Campillo, F. Bucholtz, and J. L. Dexter, "Design and characterization of long-haul single-channel intensity-modulated analog fiber-optic links," NRL Memorandum Report, NRL/MR/5650--05-8904, Sept. 2005.
[55]F. Reynaud, J. J. Alleman, and P. Connes, "Interferometric control of fiber lengths for a coherent telescope array," *App. Opt.*, vol. 31, no. 19, pp. 3736-3743, July 1992.
[56]J. J. Alleman, F. Reynaud, and P. Connes, "Fiber-linked telescope array: description and laboratory test of a two-channel prototype," *App. Opt.*, vol. 34, no. 13, pp. 2284-2294, May 1995.
[57]A. N. Bratchikov, D. I. Voskresensky, and K. van't Klooster, "Radio astronomical phased arrays with fiber-optic design architecture," *IEEE Intl. Conf. Antenna Theory Tech. Dig.*, pp. 617-623, Sept. 2003.
[58]A. N. Bratchikov, "Photonic beamforming in ultra-wideband phased antenna arrays: present state and perspectives," *Ultrawide and Ultrashort Impulse Signals*, pp. 159-164, Sept. 2006.
[59]S. M. Foreman, A. D. Ludlow, M. H. G. de Miranda, J. E. Stalnaker, S. A. Diddams, and J. Ye, "Coherent optical phase transfer over a 32-km fiber with 1 s instability at 10^{-17}," *Phys. Rev. Lett.*, 153601, Oct. 2007.
[60]J. E. Roman, M. Y. Frankel, K. J. Williams, and R. D. Esman, "Optical fiber cables for synchronous remoting of numerous transmitters/receivers," *IEEE Photon. Technol. Lett.*, vol. 10, no. 4, pp. 591-593.
[61]A. L. Campillo, E. E. Funk, D. A. Tulchinsky, J. L. Dexter, "Phase performance of an eight-channel wavelength-division-multiplexed analog-delay line," *J. Lightwave Technol.*, vol. 22, no. 2, pp. 440-447, Feb. 2004.
[62]J. W. Dreher, "Phase stability of ATA fiber optic cables," Allen Telescope Array Memo 55, http://ral.berkley.edu/ata/memos/memo55.pdf.

APPENDIX: MATLAB PROGRAM FOR CASCADE ANALYSIS

Here we present a MATLAB program to calculate the RF gain, RF noise figure, 2nd-order *SFDR* and 3rd-order *SFDR* for a cascade of *m* stages, given the RF gain, RF noise figure, *OIP*2 and *OIP*3 of each stage. Equations (1.1)-(1.4) and (1.7) are employed in the program. For instructional purposes, we write Eqs. (1.3), (1.4) and (1.7) with $n = 2$ and $n = 3$ as

$$OIP2 = \left[\sum_{\substack{i=1 \\ m\geq 2}}^{m-1} \left(OIP2_i \prod_{p=i+1}^{m} G_p \right)^{-1/2} + OIP2_m^{-1/2} \right]^{-2} \tag{A.1}$$

$$IIP2(\mathrm{dBm}) = OIP2(\mathrm{dBm}) - G(\mathrm{dB}) \tag{A.2}$$

$$SFDR_2\left(\mathrm{dB} \cdot \mathrm{Hz}^{1/2}\right) = \frac{1}{2}\left(IIP2(\mathrm{dBm}) - NF(\mathrm{dB}) + 174\right) \tag{A.3}$$

$$OIP3 = \left[\sum_{\substack{i=1 \\ m\geq 2}}^{m-1} \left(OIP3_i \prod_{p=i+1}^{m} G_p \right)^{-1} + OIP3_m^{-1} \right]^{-1} \tag{A.4}$$

$$IIP3(\mathrm{dBm}) = OIP3(\mathrm{dBm}) - G(\mathrm{dB}) \tag{A.5}$$

$$SFDR_3\left(\mathrm{dB} \cdot \mathrm{Hz}^{2/3}\right) = \frac{2}{3}\left(IIP3(\mathrm{dBm}) - NF(\mathrm{dB}) + 174\right). \tag{A.6}$$

Equations (A.2), (A.3), (A.5) and (A.6) were converted to logarithmic units for clarity. The following program is written in MATLAB 7.3.0 (R2006b).

****

```
%cascade.m calculates RF performance metrics for a cascade

clear all;

%Get inputs from user
m=input('Enter the number of stages ');
for k=1:m
    s=sprintf('Enter G_%d (dB) ', k);
    G(k)=10^(input(s)/10);
    s=sprintf('Enter NF_%d (dB) ', k);
    NF(k)=10^(input(s)/10);
    s=sprintf('Enter OIP2_%d (dBm) ', k);
    OIP2(k)=10^(input(s)/10);
    s=sprintf('Enter OIP3_%d (dBm) ', k);
    OIP3(k)=10^(input(s)/10);
end

%Calculate RF gain
Gc=10*log10(prod(G))

%Calculate RF noise figure
Gp=cumprod(G);
NFs(1)=NF(1);
for i=2:m
    NFs(i)=(NF(i)-1)/Gp(i-1);
end
NFc=10*log10(sum(NFs))

%Calculate SFDR2
Gp2=cumprod(fliplr(G));
OIP2s(m)=OIP2(m)^(-1/2);
for i=1:(m-1)
    OIP2s(i)=(OIP2(i)*Gp2(m-i))^(-1/2);
end
OIP2c=10*log10(sum(OIP2s)^(-2));
IIP2c=OIP2c-Gc;
SFDR2=(IIP2c-NFc+174)/2

%Calculate SFDR3
OIP3s(m)=OIP3(m)^(-1);
for i=1:(m-1)
    OIP3s(i)=(OIP3(i)*Gp2(m-i))^(-1);
end
OIP3c=10*log10(sum(OIP3s)^(-1));
IIP3c=OIP3c-Gc;
SFDR3=2*(IIP3c-NFc+174)/3
```

****